Novel adiabatic coupler for III-V nano-ridge laser grown on a Si photonics platform

YUTING SHI,[1] BERNARDETTE KUNERT,[2] YANNICK DE KONINCK,[2] MARIANNA PANTOUVAKI,[2] JORIS VAN CAMPENHOUT,[2] AND DRIES VAN THOURHOUT[1,*] iD

[1] *Photonics Research Group, INTEC Department, Ghent University-imec, Technologiepark-Zwijnaarde 126, 9052 Gent, Belgium*
[2] *IMEC, Kapeldreef 75, 3001 Heverlee, Belgium*
dries.vanthourhout@ugent.be

Abstract: While III-V lasers epitaxially grown on silicon have been demonstrated, an efficient approach for coupling them with a silicon photonics platform is still missing. In this paper, we present a novel design of an adiabatic coupler for interfacing nanometer-scale III-V lasers grown on SOI with other silicon photonics components. The starting point is a directional coupler, which achieves 100% coupling efficiency from the III-V lasing mode to the Si waveguide TE-like ground mode. To improve the robustness and manufacturability of the coupler, a linear-tapered adiabatic coupler is designed, which is less sensitive to variations and still reaches a coupling efficiency of around 98%. Nevertheless, it has a relatively large footprint and exhibits some undesired residual coupling to TM-like modes. To improve this, a more advanced adiabatic coupler whose geometry is varied along its propagation length is designed and manages to reach ~100% coupling and decoupling within a length of 200 μm. The proposed couplers are designed for the particular case of III-V nano-ridge lasers monolithically grown using aspect-ratio-trapping (ART) together with nano-ridge engineering (NRE) but are believed to be compatible with other epitaxial III-V/Si integration platforms recently proposed. In this way, the presented coupler is expected to pave the way to integrating III-V lasers monolithically grown on SOI wafers with other photonics components, one step closer towards a fully functional silicon photonics platform.

1. Introduction

Leveraging the well-established fabrication technology developed originally by the electronics industry, the domain of silicon photonics has seen an exponential growth over the last decade. Various passive Si optical components including highly confined waveguides (WG) [1], grating couplers [2], directional/tapered couplers [3] and arrayed waveguide gratings (AWGs) [4] as well as excellent modulators [5] and photodetectors [6] have been demonstrated. For a recent review see [7].

However, given the fact that Si has an indirect bandgap, which inhibits efficient light emission, there is a lack of high-performance optical sources directly integrated on the silicon photonics platform. Direct-bandgap III-V semiconductors, known to be efficient light emitters, could in principle fill this gap. This has motivated extensive research towards efficient approaches allowing the integration of III-V semiconductor materials on silicon, including heterogeneous integration [8,9] and hybrid integration [10]. Several groups have now also developed novel epitaxial processes providing high quality III-V materials directly grown on silicon substrates, demonstrating optically or electrically pumped lasing [11–16]. An efficient scheme for interfacing these devices with standard silicon photonics devices has not been presented yet. The preferred coupling scenario obviously depends on the approach chosen for the hetero-epitaxy process. Some groups use a thick buffer layer to reduce the III-V defect density in the active layers [13,17,18]. In that case the lasing mode is typically separated from the Si layer by several

micrometers, complicating the coupling process. Alternatively, several groups have demonstrated that it is possible to suppress defect formation by growing the III-V materials within a narrow opening defined in a SiO$_2$ mask deposited on the silicon substrate [11,15,16,19,20]. In this case the extent of the III-V structure can be considerably smaller and coupling to a waveguide directly defined in the substrate becomes feasible. E.g. L. Megalini et al. from UCSB demonstrated the growth of an InGaAsP MQW structure on a V-groove-patterned SOI substrate with its QWs ~ 500 nm away from the Si layer [16]. Y. Han et al. recently demonstrated a nanolaser array emitting at telecom wavelengths grown on SOI, with InGaAs QWs ~ 300 nm separated from the Si layer [15], while M. Wang et al have shown the growth of InGaAs/InP nanowires on an SOI substrate with the QWs ~ 500 nm away from the Si layer [19]. Z. Wang et al. demonstrated single-mode lasing of ~ 500 nm high InP nanowires grown on a Si substrate [11]. Also our previously demonstrated nano-ridge laser [20] (see Fig. 1(a)) with the active layer ~ 600 nm above the Si substrates fits this scheme. Therefore, in this paper we develop a method to design couplers that allow to integrate this type of sub-micrometer scale lasers with silicon waveguides defined in the same substrate. A simple butt-coupling approach whereby the waveguide is placed in line with the laser cavity is thereby not desired as the selective area growth process often results in irregularly shaped facets as shown in Fig. 1(b). This issue can be circumvented by coupling the light to the waveguide before it reaches the end of the III-V nano-ridge as we will discuss here. Finally it is important to note that although there are several reports on couplers for bonded heterogeneous III-V on Si integration [21–23], the requirements for monolithically integrated devices are quite different. In the case of heterogeneous integration the III-V and Si waveguide are separately defined and the design should allow for sufficient tolerance in the alignment between both layers to cope with that. In the case of monolithic integration the mask opening for growing the III-V nano-laser and the waveguide can be defined in the same patterning step as we will discuss in section 2, alleviating all issues in terms of alignment. However, since the dimensions of the III-V nano-ridge are directly determined through the epitaxial process and not through etching, the uncertainty on the precise dimensions of the III-V device might be larger than in classical structures defined through top-down processing. This influences the phase matching condition for the coupler, which has to be taken into account in the tolerance analysis. Further, due to the high index contrast, most demonstrated devices discussed above support multiple transversal modes. This makes that preventing coupling from the dominant lasing mode to undesired higher order modes is also a key requirement for the coupler.
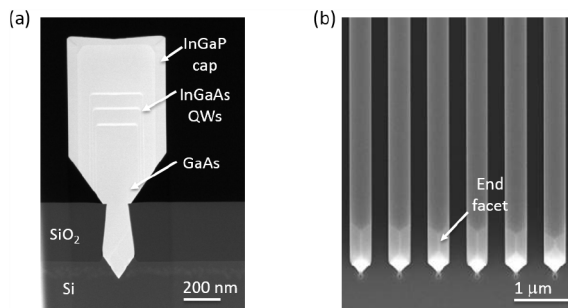
Fig. 1. (a) High-angle annular dark-field scanning transmission electron microscope (HAADF-STEM) image of the cross-section of the GaAs nano-ridge grown on Si substrate considered in this work. (b) Top-view scanning electron microscopy (SEM) images of the nano-ridge array show the irregular shape of the end facets.

In the following we will first introduce the technology platform considered and the overall design methodology. Section 3 then presents the design of a directional coupler, schematically shown in Fig. 2(a), to illustrate that efficient optical coupling between the nano-ridge laser and a

silicon waveguide is feasible. However, as the directional coupler is very sensitive to process variations, section 4 discusses the design of a more robust linearly tapered adiabatic coupler (Fig. 2(b)) with better tolerance to fabrication and wavelength variations. Finally, section 5 describes a more advanced adiabatic coupler (shown in Fig. 2(c)) whose geometry along its propagation direction is optimized to further improve the coupling efficiency and reduce the coupler length.
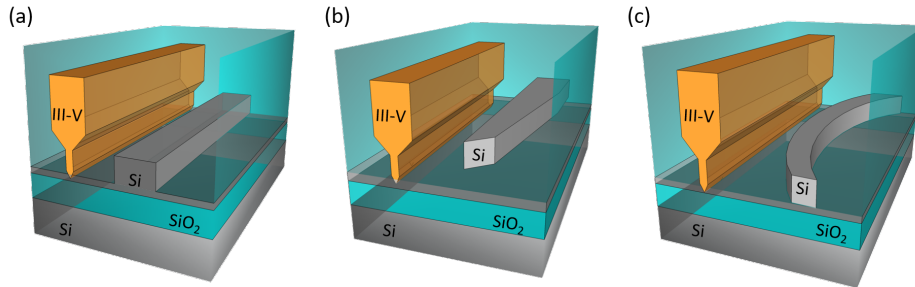

Fig. 2. 3D schematic views of the three coupler implementations. (a) Directional coupler. (b) Linearly tapered coupler. (c) Advanced adiabatic coupler.

2. Integration process and design methodology

2.1. Integration process

The proposed design approach considers the case of GaAs based nano-ridges grown on Si using the aspect ratio trapping (ART) and nano-ridge engineering (NRE) techniques described in [24,25]. A TEM image of a cross-section of such a nano-ridge grown on a standard Si substrate is shown in Fig. 1(a). Thanks to ART, defects are efficiently trapped during the growth inside narrow SiO_2 trenches . Afterwards, NRE, through controlling the growth rate on different crystal planes, allows to form box-shaped GaAs nano-ridges above the defective trenches. In principle this nano-ridge can also be grown on an SOI substrate, which would allow for the straightforward integration with Si waveguides on the same wafer. Figure 3 shows a possible process flow to fabricate such a coupler. Before III-V growth, starting from an SOI wafer, the Si ridge, which will later define the trench for III-V epitaxy, and the Si waveguide are defined are defined and planarized with SiO_2 through a standard shallow trench isolation (STI) process (Fig. 3(b)). Next the epitaxial growth of the nano-ridges can be carried out using metal-organic vapor phase epitaxy (MOVPE), the same way as we did for the structure shown in Fig. 1(a). The high-aspect-ratio trench for growing the GaAs nano-ridge can be defined using a tetramethylammonium hydroxide (TMAH) wet-etch step, resulting in exposed {111} facets at the bottom as shown in Fig. 3(c), which help suppressing anti-phase domains. The waveguide region should be protected during this step. The nano-ridge growth starts with a thin GaAs nucleation layer deposited in the trenches followed by GaAs growth inside and outside the trench (Fig. 3(d)). Afterwards, three compressively strained InGaAs QWs with about 20% indium are embedded in the fully relaxed GaAs nano-ridge, shown in Fig. 3(e). A passivation layer of InGaP covering the full ridge is deposited to suppress carrier losses through surface recombination (Fig. 3(f)). After nano-ridge growth,the whole structure can be planarized with SiO_2. Figure 4(a) shows the resulting schematic cross-section of the proposed coupler. QWs and passivation layer are not included in this sketch. In line with our previous experiments, in the remainder of the paper the thickness of the silicon layer H_{Si} is chosen to be 350 nm, and it is etched 300 nm resulting in a 50 nm remaining Si layer next to the waveguides.
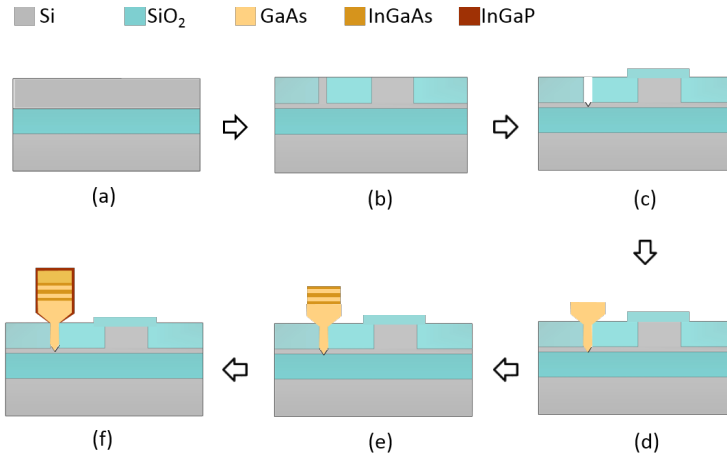
Fig. 3. Proposed process flow of the III-V/Si coupler. (a) The process starts from a SOI wafer. (b) STI process to define high aspect ratio trench and Si WG by lithographic patterning, Si dry etch and SiO$_2$ deposition and CMP (chemical-mechanical polishing). (c) Prepare SiO$_2$ trench for III-V epitaxy by Si wet etch. (d) GaAs growth inside and out side the trench. (e) The growth of three InGaAs QWs. (f) A passivation layer of InGaP is deposited to cover the nano-ridge. After this the sample is planarized with SiO$_2$, see Fig. 4(a).
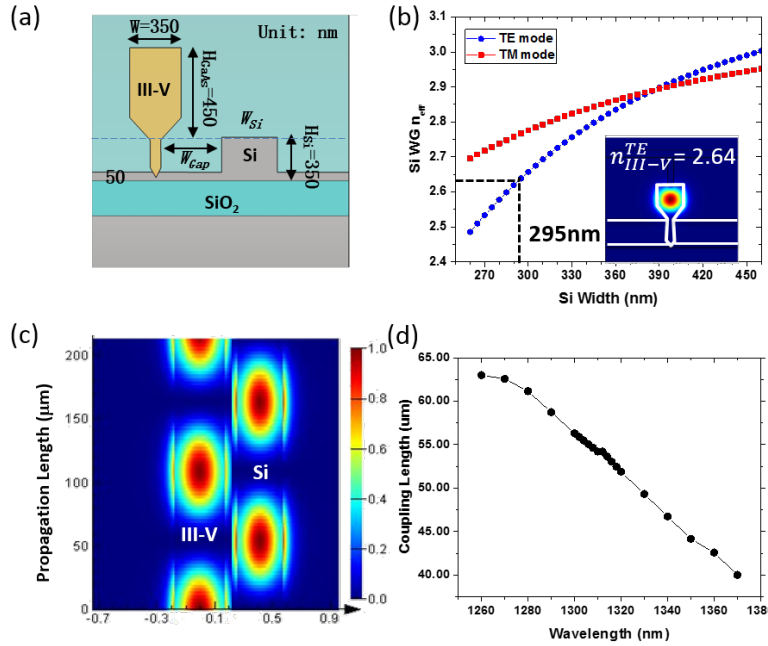
Fig. 4. (a) Schematic cross-section of the proposed coupler, consisting of the active GaAs nano-ridge and the passive Si waveguide. (b) Calculated effective refractive indices of the TE-like and TM-like ground modes of the Si WG as a function of the width W_{Si} of the Si waveguide. The insert shows the lowest order TE-like mode of the III-V nano-ridge WG. (c) 2-D top view of the optical field propagating in the coupler. (d) Coupling length and coupling efficiency as a function of wavelength.

2.2. Design methodology and simulation tools

As discussed in [20] the nano-ridge laser operates in the lowest order TE-like mode of the device. Therefore the coupler design should maximize the coupling efficiency η_C from this mode to the TE-like fundamental mode of the Si WG. Given the aforementioned fabrication process, the height of the Si waveguide is fixed ($H_{Si} = 350$ nm) and only the geometrical parameters in plane can be manipulated. Hence the free variables include the width of the Si WG W_{Si}, the spacing W_{Gap} defined as the distance between the right edge of the GaAs trench and the left edge of the Si WG and the length of the coupler L. The effective refractive index for the TE-like ground mode of this nano-ridge is calculated to be $n_{III-V}^{TE} = 2.64$ at a wavelength of 1310 nm.

All the simulations were carried out using commercial software (Lumercial MODE Solution [26]). The Finite Difference Eigenmode (FDE) solver is used to calculate the eigenmodes of the individual waveguides and within the coupler while the Bidirectional EigenMode Expansion (EME) solver is used to simulate the light propagation through the proposed couplers. We monitor the TE-like and TM-like ground modes for the standalone WGs and the lowest-order symmetric and anti-symmetric TE-like and TM-like supermodes at both input and output sides of the couplers but include 20 optical modes inside the simulation region for a good accuracy. The simulation results of the optimized linearly tapered coupler conducted by EME is confirmed by (Finite-Difference Time-Domain) FDTD simulation. Except where otherwise mentioned, all simulations were carried out for a wavelength of 1310 nm.

3. Directional coupler

In the case of the directional coupler, W_{Si} and W_{Gap} are kept constant along the propagation direction (z). The remaining free variables are hence the spacing W_{Gap} between both waveguides and the width W_{Si} of the Si waveguide. To facilitate full coupling from the TE-like lasing mode Φ_{III-V}^{TE} of the III-V nano-ridge, shown in the inset of Fig. 4(b), to the TE-like mode Φ_{Si}^{TE} of the Si WG, the two modes have to be phase-matched. In practice this means the width of the Si WG has to be chosen such that the effective refractive index n_{Si}^{TE} of its TE-like ground mode is equal to that of the TE-like ground mode of the III-V nano-ridge, $n_{III-V}^{TE} = 2.64$. From Fig. 4(b), which shows the effective indices of the first two eigenmodes of the Si WG as function of its width, we can derive this phase matching happens for $W_{Si} = W_{match} = 295$ nm (for a wavelength of 1310 nm). Figure 4(c), which shows a top view of the propagating field for $W_{Gap} = 240$ nm, proves the optical power is indeed fully exchanged between both WGs in a periodic fashion. The coupling length L_C for this configuration is 45 μm.

To obtain full field exchange in a directional coupler, the phase-matching condition has to be rigorously met and the coupler length has to be exactly equal to L_c, imposing stringent requirements to the fabrication process. The L_c is highly wavelength dependent, as shown in Fig. 4(d), decreasing from 63 μm to 40 μm in the wavelength range 1260 nm to 1360 nm. It is also found to be extremely sensitive to variations of Si WG width ΔW_{Si} and of gap ΔW_{Gap}, with $\frac{\Delta L_C}{\Delta W_{Si}} = 6.2[\mu m/nm]$ and $\frac{\Delta L_C}{\Delta W_{Gap}} = 0.354[\mu m/nm]$. This proves the directional coupler is highly sensitive to variations.

4. Linearly tapered adiabatic coupler

4.1. Proposed configuration

Given that the directional coupler exhibits a low tolerance to fabrication and temperature variations, a more robust and variation-tolerant linearly tapered adiabatic coupler is proposed. Figure 2(b) shows the proposed design. The left edge of the Si waveguide is kept parallel with the III-V nano-ridge such that W_{Gap} remains z-invariant. The right edge on the other hand is linearly varying along the coupler. The full coupler can be divided in three segments. In the first segment with length L_1 the Si waveguide starts with a sharp tip and ends with a width of W_1. It has a

slope $\frac{W_1}{L_1}$. This segment is included in the coupler to reduce perturbations introduced by the start of the Si coupler. In the second and main segment the width of the silicon waveguide varies from W_1 and expands to W_2 ($W_2 > W_1$) over a length L_2, with a slope $\frac{W_2 - W_1}{L_2}$. The variables W_1, W_2 and L_2 are the main parameters to be optimized for the coupler. The last segment consists of a straight WG with constant width W_2 to guide the coupled light away from the amplifier section, towards devices further away on the photonic IC.

The top view of the coupler and the respective TE-like optical modes at different cross-sections are shown in Fig. 5: Φ_{III-V}^{TE} is the TE-like ground mode in the standalone III-V nano-ridge, Ψ_{+1}^{TE} is the symmetric TE-like supermode at the position of W_1, Ψ_{+2}^{TE} is the symmetric TE-like supermode at the position of W_2 and finally Φ_{Si}^{TE} is the TE-like ground mode in the standalone Si WG. For easier recognition of the different modes, the symbol Φ is used to represent the modes of the standalone waveguides while Ψ is used for denoting the supermodes in the coupling region. The TM-like optical modes are supposed to be highly suppressed in the amplifier section itself but given the asymmetric structure could be excited if the coupler is not well designed. They are denoted as Φ_{III-V}^{TM} and Φ_{Si}^{TM} (in the standalone WGs) and Ψ_{+1}^{TM} and Ψ_{+2}^{TM} for the TM-like supermodes at the position W_1 and W_2.
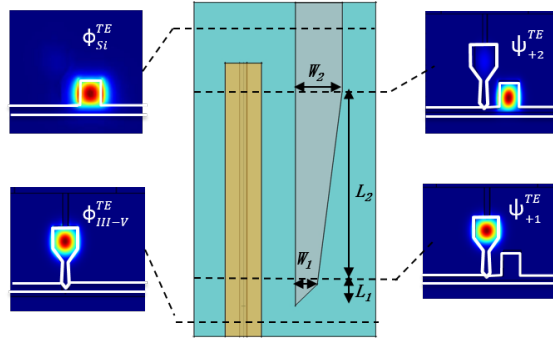

Fig. 5. Top view of the tapered coupler and the field profile of the TE-like modes at different cross-sections of the coupler.

4.2.   Optimisation of coupler width

The coupling from the III-V lasing mode Φ_{III-V}^{TE} to the Si WG mode Φ_{Si}^{TE} can be decomposed into three individual coupling processes. The initial optical mode Φ_{III-V}^{TE} in the active III-V nano-ridge is converted to Ψ_{+1}^{TE} at the start of the Si WG. The transition from Ψ_{+1}^{TE} to Ψ_{+2}^{TE} happens in the taper region. The last step is the conversion from Ψ_{+2}^{TE} to Φ_{Si}^{TE}, after which the optical field is guided further in the standalone Si WG towards following optical components. The total coupling efficiency is the product of the efficiency of each individual mode coupling process.

The widths W_1 and W_2 are optimized first. The coupling between two optical modes is approximated by taking the square of their overlap integral. Figure 6(a) shows the overlap of mode Ψ_{+}^{TE} with modes Φ_{III-V}^{TE} (solid line) and Φ_{Si}^{TE} (dashed line) as a function of W_{Si} for $W_{Gap} = 150$ nm, 240 nm and 320 nm respectively. Each set of solid and dashed lines is found to intersect around the phase-matched width $W_{si} = W_{match} = 295$ nm where the effective indices of the individual waveguide modes are equal. Note that at this crossing point, the overlap between the supermode and each standalone waveguide mode is approximately 50%.

If we define the widths $W_{\Phi_{III-V}^{TE}}$ and $W_{\Phi_{Si}^{TE}}$ as those for which the coupling efficiency from respectively the lasing mode Φ_{III-V}^{TE} and the Si WG mode Φ_{Si}^{TE} to the supermode Ψ_{+1}^{TE} is 99%,
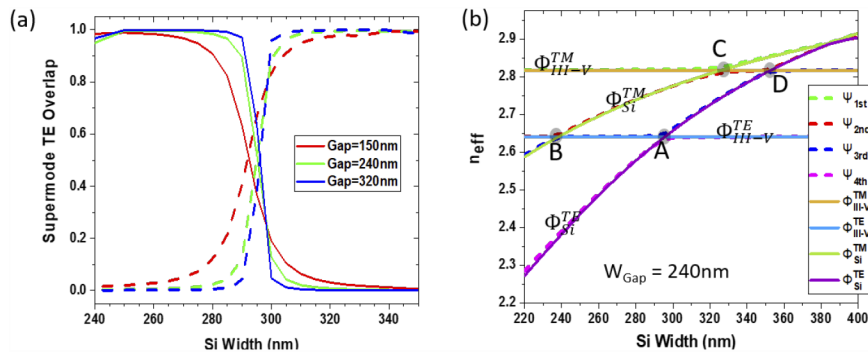
Fig. 6. (a) The overlap between TE-like supermode Ψ_+^{TE} and TE-like modes Φ_{III-V}^{TE} (solid lines) and Φ_{Si}^{TE} (dashed lines) of the standalone WGs as a function of W_{Si} for W_{Gap} = 150 nm, 240 nm and 320 nm respectively. (b) The effective refractive indices n_{neff} of the TE/TM-like ground modes of the separated III-V/Si WGs and of the first four supermodes as function of W_{Si}, for W_{Gap} = 240 nm.

W_1 and W_2 should satisfy $W_1 < W_{\Phi_{III-V}^{TE}}$ and $W_2 > W_{\Phi_{Si}^{TE}}$. For example, when W_{Gap} = 240 nm, $W_{\Phi_{III-V}^{TE}}$ = 275 nm and $W_{\Phi_{Si}^{TE}}$ = 315 nm such that $W_1 < 275$ nm and $W_2 > 315$ nm.

For the larger gap W_{Gap} = 320 nm these values can be relaxed to $W_1 < 285$ nm and $W_2 > 305$ nm while for the narrower gap W_{Gap} = 150 nm the range has to be increased to $W_1 < 235$ nm and $W_2 > 370$ nm.

In addition, coupling to the TM-like mode should be suppressed as much as possible. Figure 6(b) plots the effective refractive indices n_{eff} of the TE- and TM-like ground modes of the stand-alone III-V and Si WGs (solid lines), and of the first four supermodes (dashed lines) of the coupler for W_{Gap} = 240 nm. The overlap of a dashed line with a solid line reveals whether a supermode is rather TE-like or TM-like, and if it is centered mostly in the III-V or Si WG. Point *A* again indicates phase-matching for the modes Φ_{III-V}^{TE} and Φ_{Si}^{TE} with $W_A = W_{match}$ = 295 nm, while *B* indicates phase-matching for the modes Φ_{III-V}^{TE} and Φ_{Si}^{TM} (W_B = 235 nm), *C* for the modes Φ_{III-V}^{TM} and Φ_{Si}^{TM} (W_C = 325 nm), and *D* for the modes Φ_{III-V}^{TM} and Φ_{Si}^{TE} (W_D = 355 nm). To avoid the risk of coupling to TM-like modes, the tapered coupler should include point A but exclude B, C and D, namely $W_B < W_1 < W_A < W_2 < W_C < W_D$. Combining this set of conditions with the ones derived above we find 235 nm $< W_1 < 275$ nm and 315 nm $< W_2 < 325$ nm for W_{Gap} = 240 nm from Fig. 6. Obviously the last condition cannot be fulfilled, which means that for the narrower gaps no configuration can be defined, which at the same time assures a high coupling efficiency and low coupling to unwanted modes. This can also be seen from Table 1, which gives the allowable values for W_1 and W_2 for a wider range of values of W_{Gap} and shows that for this linearly tapered adiabatic coupler design the gap between the III-V nano-ridge and the silicon waveguide W_{Gap} has to be chosen larger than 220 nm. As we will discuss in the next section this in turns limits how compact (short) we can make the coupler.

4.3. Optimisation of coupler length

If we follow the above derived design criteria for W_1 and W_2 a high coupling efficiency should in principle be possible, at least if the lengths L_1 and L_2 are chosen sufficiently long to allow for an adiabatic transition from Ψ_{+1}^{TE} to Ψ_{+2}^{TE}.

As discussed above, the first coupler segment with length L_1 is included in the coupler to avoid scattering at the point where the Si waveguide is introduced. Simulations showed that less than 0.3% loss is introduced as soon as $L_1 > 5\,\mu$m. In the remainder of this paper, we therefore take $L_1 = 10\,\mu$m.

Table 1. Conditions imposed on W_1, W_2 (Unit: nm). The gray-colored cells indicate inconsistent conditions, excluding these values W_{Gap} for practical implementation.

Gap	W_1	W_2
150	$235 < W_1 < 235$	$370 < W_2 < 325$
200	$235 < W_1 < 260$	$330 < W_2 < 325$
240	$235 < W_1 < 270$	$315 < W_2 < 325$
280	$235 < W_1 < 280$	$310 < W_2 < 325$
320	$235 < W_1 < 285$	$305 < W_2 < 325$

The second segment with length L_2, should convert supermode Ψ_{+1}^{TE} to Ψ_{+2}^{TE} adiabatically. Therefore, we swept L_2 to optimise the coupling efficiency while keeping a compact footprint. To illustrate that a too narrow separation W_{Gap} between both waveguides will indeed introduce coupling to unwanted TM-like modes, both the simulation results for $W_{Gap} = 150$ nm and $W_{Gap} = 240$ nm are shown in Fig. 7. The parameters used in the simulations are $W_{Gap} = 150$ nm, $W_1 = 235$ nm, $W_2 = 370$ nm for Figs. 7(a)–7(c), and Figs. 7(d)–7(e) $W_{Gap} = 240$ nm, $W_1 = 270$ nm, $W_2 = 315$ nm for Figs. 7(a)–7(c). The green lines in Figs. 7(a) and 7(d) show how the coupling efficiency η_C to the desired mode Ψ_{+2}^{TE} varies as function of L_2. When $W_{Gap} = 150$ nm the coupling shows an optimum $\eta_C \sim 80\%$ for $L_2 = 150\,\mu$m. The remaining light is mostly coupled to the TM-like mode Ψ_{-2}^{TM} centered in the III-V nano-ridge. As L_2 further increases, more severe coupling between Ψ_{+2}^{TE} and Ψ_{-2}^{TM} can be seen. With W_2 close to the phase matching
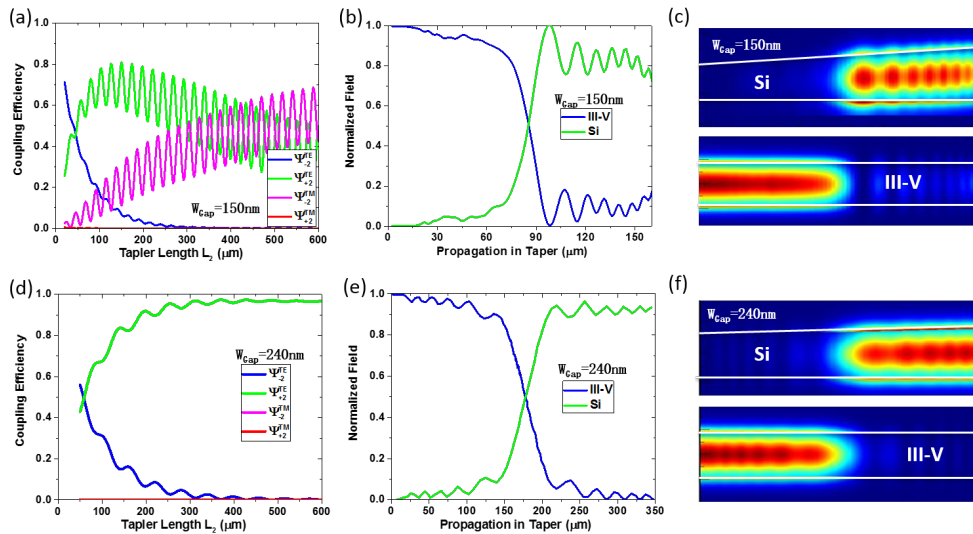
Fig. 7. Simulation results for the configurations (a)-(c) $W_{Gap} = 150$ nm, $W_1 = 235$ nm, $W_2 = 370$ nm, and (d)-(f) $W_{Gap} = 240$ nm, $W_1 = 275$ nm, $W_2 = 315$ nm. (a),(d) show the coupling to several modes as function of taper length L_2. (b),(e) depict the field exchange between the III-V nano-ridge and Si waveguide along the propagation axis for the optimised taper lengths $L_2 = 150\,\mu$m and $L_2 = 310\,\mu$m respectively. (c),(f) Show a 2-D image of the field exchange between the III-V nano-ridge and the Si waveguide for the optimised couplers.

point D for the modes Φ_{Si}^{TE} and Φ_{III-V}^{TM} as shown in Fig. 6(b), the strong coupling to Ψ_{-2}^{TM} is indeed expected. Figure 7(b) shows the evolution of the normalized field in the III-V and Si WGs respectively, when $L_2 = 150$ nm. The ripples in the second half of the taper are attributed to the interference between the modes Ψ_{+2}^{TE} and Ψ_{-2}^{TM}. The related power exchange can be observed also clearly in Fig. 7(c), which depicts the 2-D field distribution along the coupler. If the gap is increased to $W_{Gap} = 240$ nm, the maximum coupling happens at $L_2 = 310$ μm with $\eta_C \sim 98\%$ (Fig. 7(d)). In this case, the remaining $\sim 2\%$ of the optical power is partly coupled to supermode Ψ_{-2}^{TE} centered in III-V nano-ridge and partly coupled to the TM-like supermode Ψ_{+2}^{TM} centered in the Si WG. Figures 7(e) and 7(f) show how the field exchanges along the coupler when $L_2 = 310$ μm. Some ripples are still present, due to interference between the supermodes Ψ_{+2}^{TE} and Ψ_{-2}^{TE}, but they gradually decrease in amplitude along the propagation axis as the two modes get decoupled. Hence, the chosen parameters $W_{Gap} = 240$ nm, $W_1 = 275$ nm, $W_2 = 315$ nm result in good coupling efficiency and an overall decent design, albeit at the cost of larger footprint, related to the reduced coupling strength between both waveguides for this wider gap. As we now also clearly showed simply reducing the gap is not a good solution, in section 5 we will propose a more advanced design which provides a better compromise between decoupling the optical modes at the entrance and exit of the coupler on the one hand and increasing the coupling strength in the center part.

5. Advanced adiabatic coupler

Compared with the narrow-band and variation-intolerant directional coupler, the linearly tapered coupler already exhibits a broadband and more fabrication tolerant performance. Nevertheless, with a length of 310 μm its footprint is large compared to the length of a typical III-V integrated laser or amplifier ($100 - 600$ μm) and in particular with respect to our earlier demonstrated nano-ridge laser, which was only $\sim 100\mu$m long [20]. In addition insufficient decoupling at the beginning and end of the linearly tapered coupler decreases the maximum coupling efficiency and introduces extra coupling to unwanted modes, which could impact the laser performance. Therefore, a more compact adiabatic coupler design with more efficient coupling and decoupling is desired.

To improve the design, a semi-analytical approach as described in [27] is adopted. The 3D schematic view of the coupler is shown in Fig. 2(c) while the top view can be found in Fig. 8(a). Now both the width $W_{Si}(z)$ of the Si WG and the spacing $W_{Gap}(z)$ between the III-V trench and the Si WG are allowed to vary along the propagation direction. Their values are derived from optimised functions $\kappa(z)$ and $\Delta\beta(z)$ for the coupling coefficient and the dephasing between the lasing mode Φ_{III-V}^{TE} and the Si WG mode Φ_{Si}^{TE}:

$$\kappa(z) = \kappa_{max} \cdot sin\theta(z) \tag{1}$$

$$\Delta\beta(z) = -\Delta\beta_{max} \cdot cos\theta(z) \tag{2}$$

with κ_{max} the maximum coupling coefficient, at the device center $z = \frac{L}{2}$, and $\Delta\beta_{max}$ the maximum dephasing, at the beginning $z = 0$ and the end $z = L$ of the device. $\theta(z)$ is a monotonically increasing function of z, with $\theta(0) = 0$ and $\theta(L) = \pi$. The coupling coefficient κ is calculated as
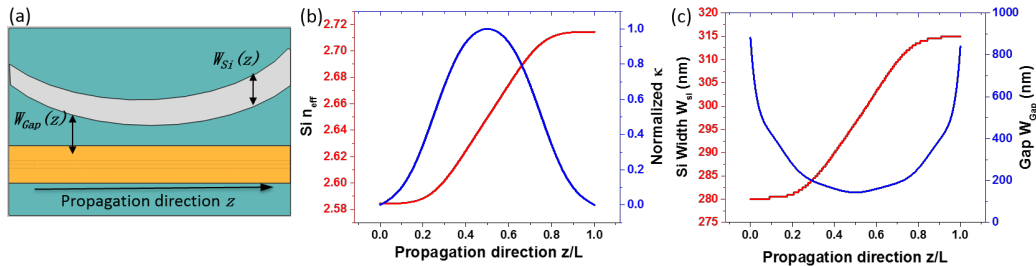
$$\kappa = \sqrt{\kappa_{12}\kappa_{21}} \tag{3}$$

$$\kappa_{12} = \frac{k_0^2}{2\beta_1} \frac{\int_{WG1}(\varepsilon_1 - \varepsilon_2)U_1^*U_2 dA}{\int |U_1|^2 dA} \tag{4}$$

$$\kappa_{21} = \frac{k_0^2}{2\beta_2} \frac{\int_{WG2}(\varepsilon_2 - \varepsilon_1)U_2^*U_1 dA}{\int |U_2|^2 dA} \tag{5}$$

with the subscripts 1 and 2 referring to the III-V nano-ridge and the Si WG respectively. k_0 is the free-space wavevector, β_i is the propagation constant of the corresponding WG, ε_i is the

permittivity function describing the waveguide profile and U_i is the TE-like optical field of the corresponding WG.

Fig. 8. (a) Top view of the optimized adiabatic coupler. The gap W_{Gap} and Si WG width W_{Gap} are functions of the propagation direction z. Note that W_{Gap} is measured from the side of the III-V trench, at the bottom of the nano-ridge, see Fig. 4. (b) The calculated effective refractive index of the Si WG n_{neff} (left axis) and normalized coupling coefficient $\frac{\kappa(z)}{\kappa_{max}}$ as functions of propagation direction z. (c) Calculated Si WG width $W_{Si}(z)$ and gap $W_{Gap}(z)$ along taper.

The maximum coupling constant κ_{max} is calculated by choosing $W_{Si}(\frac{L}{2}) = W_{match} = 295$ nm (the phase matching condition) and $W_{Gap}(\frac{L}{2}) = 150$ nm to realize a high coupling strength. Although above we found that the choice $W_{Gap} = 150$ nm introduces high coupling to unwanted modes in the linearly tapered coupler, we will show this is not the case for the optimised adiabatic coupler discussed here. $\Delta\beta(z)$ is given by:

$$\Delta\beta(z) = \frac{2\pi}{\lambda_0}(n_{III-V}^{TE} - n_{Si}^{TE}(z)) \tag{6}$$

The maximum dephasing $\Delta\beta_{max}$ occurs at the positions $z = 0$ and $z = L$, where we choose $W_{Gap}(0) = W_{Gap}(L) = 850$ nm, $W_{Si}(0) = 280$ nm and $W_{Si}(L) = 310$ nm to assure complete decoupling between both WGs.

It is found that the most efficient taper is obtained if $\theta(z)$ varies as a Blackman function [28]. We let

$$\theta(z) = \frac{\pi z}{L} - 0.25\sin\frac{2\pi z}{L} - 0.07\sin\frac{4\pi z}{L} \tag{7}$$

The values for the Si WG effective index $n_{Si}^{TE}(z)$ and the normalized coupling coefficient $\frac{\kappa(z)}{\kappa_{max}}$ optimized according to this procedure are plotted in Fig. 8(b). Figure 8(c) shows the according geometrical parameters W_{Gap} and W_{Si}. They are obtained from the known κ_{max}, $\Delta\beta_{max}$ and $\theta(z)$ using an FDE mode solver. The staircase-like pattern in the curve for $W_{Si}(z)$ in Fig. 8(c) originates from the simulation resolution of 1 nm.

Figure 9(a), shows how the coupling efficiency towards the different supermodes varies as function of L. The green curve shows how the coupling efficiency η_C towards Ψ_{+2}^{TE} firstly rapidly increases with L, and then approaches unity for $L = 150\,\mu$m and beyond while the undesired coupling towards the TM-like modes Ψ_{+1}^{TM} and Ψ_{+2}^{TM} remains low. Figures 9(b) and 9(c) show how the optical power is exchanged between both waveguides for the optimized coupler with $L = 200\,\mu$m. These results confirm the optimized adiabatic coupler allows for a high coupling efficiency and improves the coupling and decoupling processes along the taper, without spurious coupling to undesired modes.
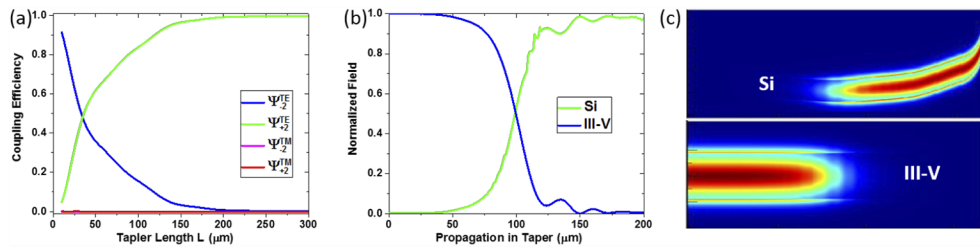
Fig. 9. Simulation results for the optimized adiabatic coupler configuration shown in Fig. 8. (a) The coupling efficiency as a function of coupler length L. A coupling efficiency $\eta_C > 99\%$ can be reached for $L = 200\,\mu m$. (b) Field exchange between III-V nano-ridge and Si waveguide along propagation direction when $W_{Si}(\frac{L}{2}) = W_{match} = 295\,nm$, $W_{Si}(0) = 280\,nm$, $W_{Si}(L) = 310\,nm$, $W_{Gap}(\frac{L}{2}) = 150\,nm$, $W_{Gap}(0) = W_{Gap}(L) = 820\,nm$, $L = 200\,\mu m$. (c) 2-D image of field exchange between III-V nano-ridge and Si waveguide for $L = 200\,\mu m$.

6. Tolerance to fabrication variations

As the III-V nano-ridges are developed for lasing in the O-band, the couplers are expected to have high coupling efficiency over the $1260 - 1360\,nm$. Further, in our fabrication process, the exact size of the III-V nano-ridge is determined by the epitaxy process. A change in growth temperature, growth time or mask loading might cause slight deviations in the nano-ridge dimensions. Therefore, the tolerance to wavelength and fabrication variations of the three coupler implementations is discussed in this section.

Figure 10 shows how the coupling efficiency of the three couplers varies versus wavelength. For the directional coupler, even though 100% coupling efficiency is achieved at $\sim 1310\,nm$, η_c rapidly drops away from this central wavelength, by 37% at 1260 nm. To the contrary, the variations in coupling efficiency is only $\sim 4\%$ and $\sim 2\%$ for the linearly tapered coupler and the advanced adiabatic coupler respectively over a 100 nm wide wavelength range, proving their broadband character. This follows from the fact that, although n_{III-V}^{TE} varies relatively strongly with wavelength (shown in Fig. 10), the deviation from the phase matching condition remains small as also the effective index of the silicon waveguide decreases with wavelength.
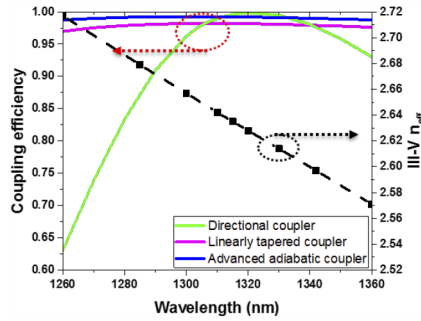
Fig. 10. Coupling efficiency (left axis) and effective refractive index n_{III-V}^{TE} (right axis) as a function of wavelength.

Figures 11(a) and 11(b) plot the coupling efficiency η_C as function of a deviation in height ΔH or width ΔW of the nano-ridge dimensions for the linearly tapered coupler with $W_{Gap} = 240\,nm$, $W_1 = 275\,nm$, $W_2 = 315\,nm$, $L_1 = 10\,\mu m$, $L_2 = 310\,\mu m$ and the advanced adiabatic coupler with $L = 200\,\mu m$. A 30 nm variation in III-V nano-ridge height causes the coupling efficiency drop from 98% to $\sim 80\%$ for both couplers. Figure 11(b) shows that 10 nm variation in width is

acceptable with η_C decreasing by $\sim 20\%$. But for width variations above 30 nm the coupling efficiency drastically drops. The different impact from the nano-ridge height and width variations on the coupling efficiency can be understood by the related changes in the effective index of the nano-ridge. n_{III-V}^{TE} is more strongly influenced by width variations than by height variations. These simulations indicate that the linearly tapered coupler and the advance adiabatic coupler are strongly improved in terms of fabrication tolerances with respect to the directional coupler. Although the tolerance of the advanced adiabatic coupler is slightly worse than that of the longer linearly tapered adiabatic coupler, it allows the freedom to optimise either towards compact size or towards high processing tolerance, dependent on the application.
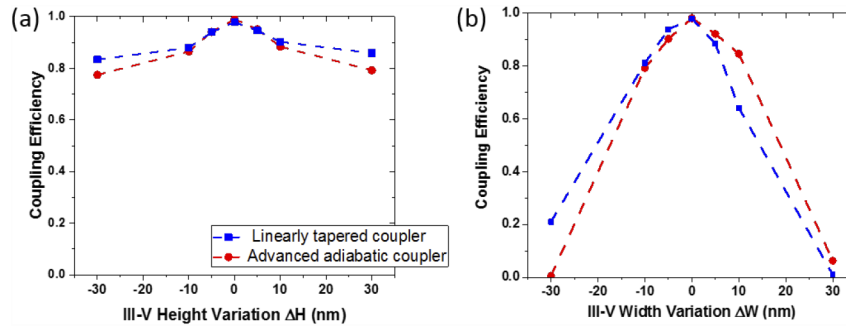
Fig. 11. Coupling efficiency as a function of (a) nano-ridge height variation, (b) width variation.

7. Conclusion

We proposed a novel adiabatic coupler working in the O-band for coupling light from a III-V nano-ridge laser to a Si waveguide. The coupler is compatible with our earlier presented process for the monolithic epitaxy of GaAs based nano-ridges on silicon using the aspect ratio trapping combined with nano-ridge engineering. We showed that a directional coupler design can reach a coupling efficiency of 100% but is very sensitive to process and wavelength variations. To improve this, a more robust linearly tapered adiabatic coupler is presented, which is more tolerant to process variations and can still achieve a 98% coupling efficiency. However, this comes at the cost of an increased footprint and some residual coupling to unwanted modes. To prevent this undesired coupling from influencing the laser operation, a more advanced adiabatic couple, which better decouples the modes at the beginning and end of the coupler was then proposed. This device exhibits a coupling efficiency >99% at 1310 nm and >97% over the full O-band, for a coupler length of 200 μm, without coupling to undesired modes. Ultimately the objective is to allow for electrical injection of these devices. The necessary metal contacts should thereby be implemented without introducing excessive loss, e.g. through separating them from the nano-ridges by a narrow fin [29]. In such a case, the optical modes of the nano-ridge should hardly be affected and the design procedure outlined above would remain applicable. Finally it is important to note that the design procedure proposed here can directly be transferred to other III-V nano-lasers epitaxially grown on silicon recently proposed in literature [11,15,16,19].

The presented adiabatic coupler is expected to connect III-V devices with the whole on-chip Si photonics circuit. Besides, it helps explore the potential of the epitaxial III-V to make more complex and functional devices with the help of external Si circuits to provide feedback or/and form a cavity.

Funding

Acknowledgments

Disclosures

The authors declare no conflicts of interest.

References

1. U. Fischer, T. Zinke, J.-R. Kropp, F. Arndt, and K. Petermann, "0.1 dB/cm waveguide losses in single-mode SOI rib waveguides," IEEE Photonics Technol. Lett. **8**(5), 647–648 (1996).
2. D. Taillaert, P. Bienstman, and R. Baets, "Compact efficient broadband grating coupler for silicon-on-insulator waveguides," Opt. Lett. **29**(23), 2749–2751 (2004).
3. P. Trinh, S. Yegnanarayanan, and B. Jalali, "Integrated optical directional couplers in silicon-on-insulator," Electron. Lett. **31**(24), 2097–2098 (1995).
4. W. Bogaerts, P. Dumon, D. Van Thourhout, D. Taillaert, P. Jaenen, J. Wouters, S. Beckx, V. Wiaux, and R. G. Baets, "Compact wavelength-selective functions in silicon-on-insulator photonic wires," IEEE J. Sel. Top. Quantum Electron. **12**(6), 1394–1401 (2006).
5. T.-Y. Liow, K.-W. Ang, Q. Fang, J.-F. Song, Y.-Z. Xiong, M.-B. Yu, G.-Q. Lo, and D.-L. Kwong, "Silicon modulators and germanium photodetectors on SOI: monolithic integration, compatibility, and performance optimization," IEEE J. Sel. Top. Quantum Electron. **16**(1), 307–315 (2010).
6. S. J. Koester, J. D. Schaub, G. Dehlinger, and J. O. Chu, "Germanium-on-SOI infrared detectors for integrated photonic applications," IEEE J. Sel. Top. Quantum Electron. **12**(6), 1489–1502 (2006).
7. "December 2018 special issue: Silicon photonics | proceedings of the ieee." https://proceedingsoftheieee.org/view-recent-issues/december-2018/. Accessed: 25-Mar-2019.
8. J. Van Campenhout, P. Rojo-Romeo, P. Regreny, C. Seassal, D. Van Thourhout, S. Verstuyft, L. Di Cioccio, J.-M. Fedeli, C. Lagahe, and R. Baets, "Electrically pumped InP-based microdisk lasers integrated with a nanophotonic silicon-on-insulator waveguide circuit," Opt. Express **15**(11), 6744–6749 (2007).
9. Z. Wang, A. Abbasi, U. Dave, A. De Groote, S. Kumari, B. Kunert, C. Merckling, M. Pantouvaki, Y. Shi, B. Tian, K. Van Gasse, J. Verbist, R. Wang, W. Xie, J. Zhang, Y. Zhu, J. Bauwelinck, X. Yin, Z. Hens, J. Van Campenhout, B. Kuyken, R. Baets, G. Morthier, D. Van Thourhout, and G. Roelkens, "Novel light source integration approaches for silicon photonics," Laser Photonics Rev. **11**(4), 1700063 (2017).
10. D. Liang, G. Roelkens, R. Baets, and J. Bowers, "Hybrid integrated platforms for silicon photonics," Materials **3**(3), 1782–1802 (2010).
11. Z. Wang, B. Tian, M. Pantouvaki, W. Guo, P. Absil, J. Van Campenhout, C. Merckling, and D. Van Thourhout, "Room-temperature InP distributed feedback laser array directly grown on silicon," Nat. Photonics **9**(12), 837–842 (2015).
12. S. Chen, W. Li, J. Wu, Q. Jiang, M. Tang, S. Shutts, S. N. Elliott, A. Sobiesierski, A. J. Seeds, I. Ross, P. M. Smowton, and H. Liu, "Electrically pumped continuous-wave III–V quantum dot lasers on silicon," Nat. Photonics **10**(5), 307–311 (2016).
13. Y. Wan, J. Norman, Q. Li, M. Kennedy, D. Liang, C. Zhang, D. Huang, Z. Zhang, A. Y. Liu, A. Torres, D. Jung, A. C. Gossard, E. L. Hu, K. M. Lau, and J. E. Bowers, "1.3 μm submilliamp threshold quantum dot micro-lasers on Si," Optica **4**(8), 940–944 (2017).
14. Y. Han, W. K. Ng, C. Ma, Q. Li, S. Zhu, C. C. Chan, K. W. Ng, S. Lennon, R. A. Taylor, K. S. Wong, and K. M. Lau, "Room-temperature InP/InGaAs nano-ridge lasers grown on Si and emitting at telecom bands," Optica **5**(8), 918–923 (2018).
15. Y. Han, W. K. Ng, Y. Xue, Q. Li, K. S. Wong, and K. M. Lau, "Telecom InP/InGaAs nanolaser array directly grown on (001) silicon-on-insulator," Opt. Lett. **44**(4), 767–770 (2019).
16. L. Megalini, B. Bonef, B. C. Cabinian, H. Zhao, A. Taylor, J. S. Speck, J. E. Bowers, and J. Klamkin, "1550-nm InGaAsP multi-quantum-well structures selectively grown on v-groove-patterned SOI substrates," Appl. Phys. Lett. **111**(3), 032105 (2017).
17. H. Choi, C. Wang, and N. Karam, "GaAs-based diode lasers on Si with increased lifetime obtained by using strained InGaAs active layer," Appl. Phys. Lett. **59**(21), 2634–2635 (1991).
18. M. E. Groenert, C. W. Leitz, A. J. Pitera, V. Yang, H. Lee, R. J. Ram, and E. A. Fitzgerald, "Monolithic integration of room-temperature cw GaAs/AlGaAs lasers on Si substrates via relaxed graded GeSi buffer layers," J. Appl. Phys. **93**(1), 362–367 (2003).

19. M. Wang, Z. Li, X. Zhou, Y. Li, P. Wang, H. Yu, W. Wang, and J. Pan, "InGaAs/InP multi-quantum-well nanowires directly grown on SOI substrates and optical property characterizations," in *CLEO: Applications and Technology* (Optical Society of America, 2018), pp. JTh2A–76.

20. Y. Shi, Z. Wang, J. Van Campenhout, M. Pantouvaki, W. Guo, B. Kunert, and D. Van Thourhout, "Optical pumped InGaAs/GaAs nano-ridge laser epitaxially grown on a standard 300-mm Si wafer," Optica **4**(12), 1468–1473 (2017).

21. A. W. Fang, E. Lively, Y.-H. Kuo, D. Liang, and J. E. Bowers, "A distributed feedback silicon evanescent laser," Opt. Express **16**(7), 4413–4419 (2008).

22. M. Lamponi, S. Keyvaninia, C. Jany, F. Poingt, F. Lelarge, G. De Valicourt, G. Roelkens, D. Van Thourhout, S. Messaoudene, J.-M. Fedeli, and G. Duan, "Low-threshold heterogeneously integrated InP/SOI lasers with a double adiabatic taper coupler," IEEE Photonics Technol. Lett. **24**(1), 76–78 (2012).

23. S. Dhoore, S. Uvin, D. Van Thourhout, G. Morthier, and G. Roelkens, "Novel adiabatic tapered couplers for active III-V/SOI devices fabricated through transfer printing," Opt. Express **24**(12), 12976–12990 (2016).

24. B. Kunert, W. Guo, Y. Mols, R. Langer, and K. Barla, "Integration of III/V hetero-structures by selective area growth on Si for nano-and optoelectronics," ECS Trans. **75**(8), 409–419 (2016).

25. S. Lourdudoss, J. Bowers, and E. C. Jagadish, *Future Directions in Silicon Photonics*, vol. 101 (Elsevier, 2019).

26. "Lumerical official website," https://www.lumerical.com/. Accessed: 2010-09-30.

27. H. Ishikawa, "Fully adiabatic design of waveguide branches," J. Lightwave Technol. **25**(7), 1832–1840 (2007).

28. H.-k. Hsiao, K. A. Winick, and J. D. Monnier, "Midinfrared broadband achromatic astronomical beam combiner for nulling interferometry," Appl. Opt. **49**(35), 6675–6688 (2010).

29. Y. De Koninck, G. Roelkens, and R. Baets, "Electrically pumped 1550 nm single mode iii-v-on-silicon laser with resonant grating cavity mirrors," Laser Photonics Rev. **9**(2), L6–L10 (2015).